

## Effects of Remote Generation Sites on Model Estimates of $M_2$ Internal Tides in the Philippine Sea\*

COLETTE G. KERRY, BRIAN S. POWELL, AND GLENN S. CARTER

*University of Hawaii at Manoa, Honolulu, Hawaii*

(Manuscript received 3 May 2012, in final form 13 September 2012)

### ABSTRACT

This study investigates the impact of remotely generated internal tides on model estimates of barotropic to baroclinic tidal conversion for two generation sites bounding the Philippine Sea: the Luzon Strait and the Mariana Island Arc. A primitive equation model is used to characterize the internal tides generated by the principal semidiurnal tide ( $M_2$ ) over a domain encompassing the two generation sites. Energetic internal tides are generated at the Luzon Strait where nearly 17 GW of barotropic tide energy is converted to baroclinic energy, of which 44% (4.78 GW) is radiated eastward into the Philippine Sea. From the Mariana Arc, baroclinic energy propagates westward into the Philippine Sea as a result of 3.82 GW of barotropic to baroclinic energy conversion. Simulations that focus on each generation site without influence of the other are performed, and comparisons show that remotely generated internal tides have a significant effect on local conversion at the two sites. Total conversion is greater in the absence of remotely generated internal tides at both sites: 11% greater at the Luzon Strait and 65% greater at the Mariana Arc. The first three modes of the remotely generated internal tides traverse the basin and alter the amplitude and phase of bottom pressure. The arrival of the remote internal tides varies significantly with changing stratification and mesoscale circulation. The results suggest that an important source of variability in local conversion around the globe is due to remotely generated internal tides.

### 1. Introduction

The Philippine Sea is bounded by two significant barotropic to baroclinic tide conversion sites: the Mariana Island Arc to the east and the Luzon Strait to the west. Particularly energetic internal tides are generated at the Luzon Strait as the barotropic tidal flow is forced between two islands and over steep topography associated with the ridge system, producing one of the strongest internal tide regimes observed worldwide. This baroclinic energy propagates both westward into the South China Sea (SCS) and eastward into the Philippine Sea. At the eastern margin of the Philippine Sea, baroclinic tides generated at the Mariana Arc propagate westward into the Philippine Sea.

---

\* School of Ocean and Earth Science and Technology Publication 8746.

Corresponding author address: Colette Kerry, Dept. of Oceanography, University of Hawaii at Manoa, 1000 Pope Rd., Honolulu, HI 96822.  
E-mail: ckerry@hawaii.edu

The study of internal tides at deep ocean topographies is motivated by their role in the dissipation of the surface tides in the open ocean (Egbert and Ray 2000, 2001), their potentially important role in mixing of the deep oceans (Munk and Wunsch 1998), and the impacts of shoaling and breaking internal tides incident on continental slopes (Holloway 1987; Klymak et al. 2007, 2010; Farmer et al. 2011). Using satellite altimetry to estimate tidal dissipation throughout the world's oceans, Egbert and Ray (2001) found that up to one-third of the surface tide loss occurs in the open ocean, rather than to bottom friction in shallow seas as had been traditionally assumed (Jefferies 1920). Turbulent dissipation of internal tide energy in the deep oceans may provide approximately half of the mixing required to maintain the thermohaline circulation (Munk and Wunsch 1998). Understanding the generation and propagation of internal tides and the extent of local versus remote dissipation is important in understanding the energy budget of the abyssal ocean and developing mixing parameterizations for global circulation models. At the Luzon Strait, local baroclinic energy dissipation may be an important turbulent energy source for the mixing of the Kuroshio and SCS waters.

The generation of internal tides in the open ocean occurs at isolated regions of steep topography. Simmons et al. (2004) used a global tidal simulation to identify 20 internal tide generation sites covering 10% of the seafloor that account for approximately 75% of the conversion from barotropic to baroclinic tides in the global oceans. Using a numerical simulation of the  $M_2$  tide in the Pacific Ocean, Niwa and Hibiya (2001) found that 84% of the conversion from barotropic to baroclinic tidal energy occurred at prominent topographic features such as island chains, oceanic ridges, and the continental shelf slope in the East China Sea. These isolated generation regions include the Luzon Strait and the Mariana Island Arc that are the focus of this study.

Remotely generated internal tides have been shown to produce changes in the local internal tide generation (Kelly and Nash 2010; Zilberman et al. 2011; Hall and Carter 2011; Powell et al. 2012). As shown in Fig. 13 of Simmons et al. (2004), there are many regions around the globe where remote energy fluxes reach local conversion sites. Remote effects on local generation are related to a change in phase of the bottom pressure perturbation with respect to the local surface tide. What is less well known is how significantly remotely generated internal waves influence the local tidal conversion.

In the Luzon Strait, strong internal tides with vertical isopycnal displacements of up to 150 m have been observed (Duda et al. 2004; Ramp et al. 2004), and baroclinic energy fluxes of up to  $60 \text{ kW m}^{-1}$  have been measured (Alford et al. 2011). Zhao et al. (2004) observe internal wave packets from satellite images propagating northwestwards from the Luzon Strait into the SCS, where Lien et al. (2005), using ADCP measurements, report nonlinear waves are predominately at semidiurnal periods. Alford et al. (2010) use observations from a series of moorings to infer the evolution of nonlinear internal waves as they propagate into the SCS and interact with the continental slope. Little attention has been given however to the internal tides that propagate eastward from the Luzon Strait into the Philippine Sea. At the eastern margin of the Philippine Sea, Zhao and D'Asaro (2011) use satellite altimeter data and estimate baroclinic energy fluxes of up to  $17 \text{ kW m}^{-1}$  propagating westward from the Mariana Island Arc in a focused beam. Observations of internal tides in the Philippine Sea are sparse in time and space. Numerical modeling allows us to place these observations in a dynamical setting, better understand the source and propagation of the internal tides, and make regional estimates of barotropic to baroclinic energy conversion, baroclinic energy fluxes and dissipation rates.

Several modeling studies have been undertaken in the region; however, the estimates of the energy converted

vary significantly. Niwa and Hibiya (2004) investigated the  $M_2$  internal tide generation for a domain including the Luzon Strait and the East China Sea. Using annual mean stratification, they predicted the total barotropic to baroclinic tidal energy conversion at the Luzon Strait to be 14 GW, with 27% of the incident barotropic energy being converted. Using a linear damping scheme, they found 53% of the energy converted (7.4 GW) propagates as baroclinic tides into the SCS (4.2 GW) and the Philippine Sea (3.2 GW) with the remaining 6.6 GW dissipated locally. Jan et al. (2008) simulated the internal tide generation using four principal constituents ( $O_1$ ,  $K_1$ ,  $M_2$ , and  $S_2$ ) at the Luzon Strait. Approximately 30% of the incident  $M_2$  barotropic tidal energy was converted to the internal tides. Barotropic to baroclinic energy conversion for the  $M_2$  tide was 9.6 GW, supporting a total  $M_2$  baroclinic energy flux away from the ridge of 5.05 GW (3.02 GW to the west and 2.30 to the east), leaving 47% dissipated locally. Conversion values for runs with all four constituents ranged from 11 to 50 GW over the spring-neap cycle. Alford et al. (2011) calculate a total modeled conversion over the Luzon Strait, for semidiurnal and diurnal bands, of 24.1 GW, with 39% local dissipation. Simmons et al. (2004) use four different modeling approaches and present conversion values ranging from 9–22 GW for this same region.

There are a variety of reasons for this differentiation in conversion estimates, including different parameterizations of unresolved physical processes and sensitivities to bathymetry and stratification that are discussed in detail in Di Lorenzo et al. (2006). Conversion estimates may vary significantly with different vertical and horizontal model resolutions and are highly sensitive to bathymetric smoothing which is often required in  $s$ -coordinate ocean models. Model estimates of tidal dissipation are uncertain as subgrid-scale processes must be parameterized. In this paper, we show that the inclusion—or not—of remotely generated internal tides in models may be a significant source of variability in estimates of conversion.

In this paper, we investigate the tidal conversion at the Luzon Strait and the Mariana Island Arc and the influence that each exerts on the other. We characterize the combined case and compare this to local generation at each of the two sites without the effects of internal tides from the other. Remotely generated internal tides are found to significantly influence local barotropic to baroclinic tidal conversion at both the Luzon Strait and Mariana Arc generation sites. In particular, internal tides generated at the Luzon Strait are found to profoundly alter conversion at the Mariana Arc.

## 2. Model description

We use the regional ocean modeling system (ROMS) to simulate the principal lunar, semidiurnal ( $M_2$ ) tide in the Philippine Sea. ROMS is a free-surface, hydrostatic, primitive equation ocean model solved on a curvilinear grid with a terrain-following vertical coordinate system (Shchepetkin and McWilliams 2005). For computational efficiency, ROMS uses a split-explicit time-stepping scheme allowing the barotropic solution to be computed at a much smaller time step than is used for the (slow-mode) baroclinic equations using a temporal-averaging filter to ensure preservation of tracers and momentum and minimize aliasing of unresolved barotropic signals into the baroclinic motions (Shchepetkin and McWilliams 2005). The ROMS computational kernel is further described in Shchepetkin and McWilliams (1998, 2003). Although internal tides inherently have a non-hydrostatic component, the hydrostatic approximation remains valid for the relatively large-scale processes and coarse model resolution used in this study, as shown in Bergh and Berntsen (2009) and Vitousek and Fringer (2011). While the internal tides in the SCS have been shown to be highly nonlinear and nonhydrostatic as they steepen on interaction with the continental shelf (Alford et al. 2010; Farmer et al. 2011), we focus only on the propagation into the Philippine Sea where the internal tides travel into deep water. Hydrostatic models have been used in many regional and global scale internal tide studies (e.g., Merrifield and Holloway 2002; Niwa and Hibiya 2004; Simmons et al. 2004; Carter et al. 2008; Jan et al. 2008; Zilberman et al. 2009; Powell et al. 2012).

To investigate the effect of remotely generated internal tides on local generation at both the Luzon Strait and the Mariana Island Arc we perform simulations using three different domain sizes, as shown in Fig. 1. The large domain, hereafter referred to as the FULL case, extends from the SCS to the east of the Mariana Arc, including both the Luzon Strait and Mariana Arc tidal conversion sites. The LUZON domain shares the same boundaries as the FULL case to the west, north, and south but has its eastern boundary at 137.85°E (the dot-dashed line in Fig. 1) to remove the influence of baroclinic tides originating from the Mariana Arc. Similarly, the MARIANA domain is used to simulate the tides from the Mariana Arc without the influence of the internal tides from the Luzon Strait, and its western boundary is at 128.48°E (the dashed line in Fig. 1). The model has a variable horizontal resolution, with 8 km over most of the domain, and a higher zonal resolution of 4.5 km over the Luzon Strait. This allows improved bathymetric resolution while minimizing pressure gradient errors in the region of steep topography. The model is configured with 25 vertical s-layers distributed

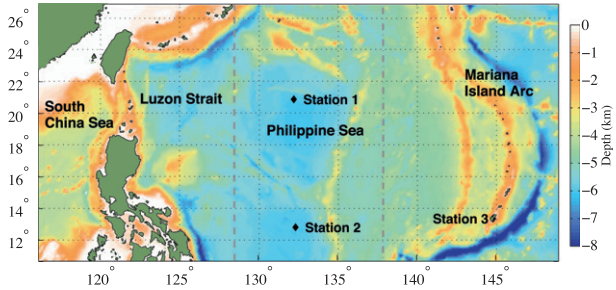


FIG. 1. FULL model domain with bathymetry showing the three tidal stations used for model verification. The gray dash-dot line shows the eastern boundary of the LUZON domain, and the gray-dashed line shows the western boundary of the MARIANA domain. Note the two domains overlap.

with a higher resolution in the upper 250 m of the water column. The Large et al. (1994)  $K$ -profile interior closure scheme is used in parameterizing vertical turbulent mixing of momentum and tracers. Harmonic mixing of momentum is applied in the horizontal to handle subgrid-scale turbulence and the viscosity is derived from the horizontal divergence of the deviatoric stress tensor (Wajsowicz 1993). The parameters are scaled by grid-size such that less explicit diffusion occurs in the high-resolution (4.5 km) region than in the 8 km region.

In models using terrain-following coordinate systems, steep topographic gradients generate numerical errors associated with the computation of the pressure gradient term resulting in artificial along-slope flows (Haney 1991; Mellor et al. 1994). These errors depend on the topographic steepness and the intensity of the stratification (Haidvogel et al. 2000). ROMS is effective at minimizing these horizontal pressure gradient (HPG) errors (Shchepetkin and McWilliams 2003); although, a certain degree of topographic smoothing is usually still desirable. The generation of internal tides occurs primarily at regions of steep topography and is highly sensitive to bathymetric smoothing (Di Lorenzo et al. 2006). For this study, a smoothing method has been applied in which a high priority is placed on maintaining topography (slopes and peak heights) important for internal tide generation while attempting to minimize HPG errors. We accomplish this by utilizing a linear programming technique described in Sikiric et al. (2009). The model bathymetry is obtained from the General Bathymetric Chart of the Oceans one-minute gridded bathymetry data generated from combined satellite-derived gravity data and ship depth soundings (Intergovernmental Oceanographic Commission 2003).

The model simulations are performed with horizontally uniform stratification using the spatial mean across the domain of the annual mean climatology from the National Oceanographic Data Center's World Ocean

TABLE 1. Comparisons of  $M_2$  surface amplitudes and phases between the model and sea level gauges. Phase is relative to the equilibrium tide at Greenwich,  $E$  is defined in Eq. (1).

	Amplitude (m)	Phase	$E$ (m)	$E$ (%)
Station 1				
ROMS	0.45	292.19	0.047	9.5
Observed	0.49	285.71		
Station 2				
ROMS	0.52	289.34	0.025	4.5
Observed	0.55	290.98		
Station 3				
ROMS	0.17	267.94	0.042	38.5
Observed	0.11	271.50		

Atlas. The FULL model is forced at the four open boundaries with tidal surface elevation and momentum from the global barotropic tidal model provided by the Oregon State University Ocean Topography Experiment (TOPEX)/Poseidon Global Inverse Solution (TPXO6.2) (Egbert and Erofeeva 2002). To make valid comparisons of internal tide generation with the LUZON and MARIANA domains, it was important to ensure that the coincident barotropic energy fluxes at the western and eastern boundaries of the smaller domains matched the barotropic fluxes in the FULL model run. The LUZON domain was therefore forced at its eastern boundary by surface elevation and barotropic flow extracted from the FULL model run, and by TPXO at its western, northern and southern boundaries. Similarly, the western boundary forcing for the MARIANA domain was derived from surface elevation and barotropic flow from the FULL run, and by TPXO at its remaining boundaries. The Chapman condition (Chapman 1985) is applied to the free surface at the boundaries and the Flather condition (Flather 1976) is applied to the barotropic velocity so that barotropic energy is transmitted out of the domain. Baroclinic energy is absorbed at the boundaries using a flow relaxation scheme involving a 130 km wide sponge layer (roughly twice the Rossby radius for this latitude) over which viscosity and diffusivity are increased linearly by an order of magnitude from the values applied within the model domain. The model is run for a period of 64 days and the 6 tidal cycles (74.52 h) following the first 60 days are used in the analysis.

### 3. Results

#### a. $M_2$ surface tide field

We begin by comparing the results of the FULL case with observations and examining the tidal properties. Observed surface elevation data is available at three sea level stations within the model domain, as marked in Fig. 1. The two deep water stations (Stations 1 and 2) are Deep-Ocean Assessment and Reporting of Tsunamis (DART) buoys

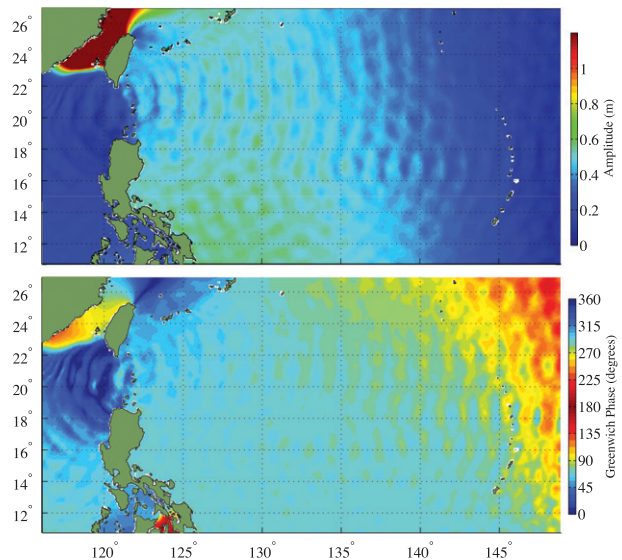


FIG. 2.  $M_2$  cotidal plot showing (top) amplitude and (bottom) Greenwich phase for the FULL case.

maintained by the National Oceanic and Atmospheric Administration (NOAA) National Data Buoy Center. Station 3 is a coastal tidal station located in Pago Bay, Guam, available from the NOAA Center for Operational Oceanographic Products and Services. The modeled and observed amplitudes and phases of the  $M_2$  tide are given in Table 1. A quantitative comparison accounting for both amplitude and phase is given using an absolute RMS error, as described by Cummins and Oey (1997),

$$E = \sqrt{\frac{1}{2}(A_o^2 + A_m^2) - A_o A_m \cos(G_o - G_m)}, \quad (1)$$

where subscripts  $o$  and  $m$  denote observed and modeled amplitudes ( $A$ ) and phases ( $G$ ), respectively.

The model shows good agreement with the observed values at the deep water stations. Station 3 is a coastal station and is poorly resolved by the 8-km resolution of the model owing to the steep topography of the region. The corresponding model grid cell depth is 900 m, as compared to the true depth of 8 m for the station. The amplitude and phase of the  $M_2$  surface elevation is altered by the generation of internal tides in the baroclinic solution. The surface expression of the internal tides introduces small-scale variability with wavelengths of 170 km, as shown by the cotidal plot in Fig. 2. This compares with wavelengths between 150 and 200 km shown in modeling studies by Niwa and Hibiya (2004) and a wavelength of 120 km by Jan et al. (2008).

The  $M_2$  tide causes strong barotropic velocities as it moves over the shallow ridges of the Luzon Strait. The Strait's bathymetry is characterized by two ridges that lie in

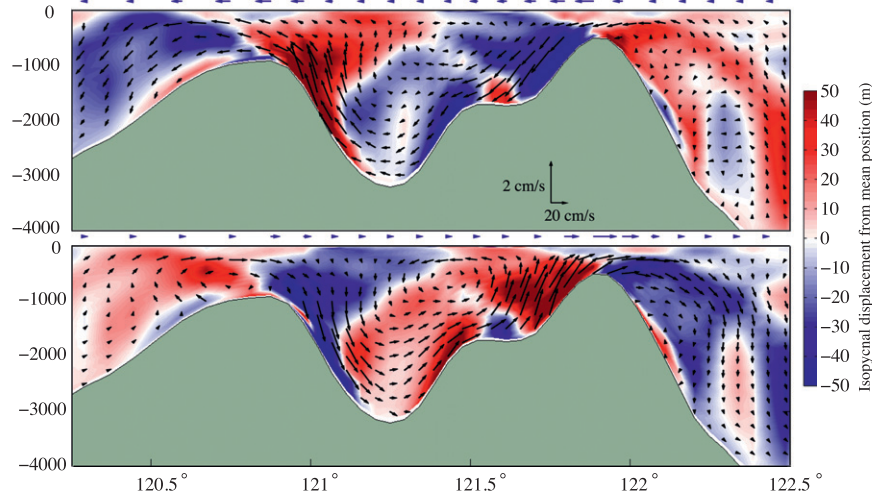


FIG. 3. Instantaneous isopycnal displacement at a cross section through 21°N at the Luzon Strait, for (top) maximum westward barotropic flow and (bottom) maximum eastward barotropic flow. Baroclinic velocities are shown by the black arrows. Barotropic flow is shown by the blue arrows above each plot.

an approximately north–south direction; the eastern ridge is the shallowest with depths of 500–1500 m and contains the Batanes Islands, while the western ridge extends directly south from Taiwan and rejoins with the eastern ridge in the southern portion of the Strait. At the Luzon Strait, barotropic velocities along the major axes reach 15–25 cm s<sup>-1</sup> across the eastern ridge, and 20–25 cm s<sup>-1</sup> at the western ridge. Our modeled  $M_2$  tidal ellipse parameters are in good agreement with the ADCP measured values from a mooring located at 21°N, 120.5°E reported by Liao et al. (2010). The measured major axis velocity and phase were 8.46 cm s<sup>-1</sup> and 224.09°, respectively, compared to 8.65 cm s<sup>-1</sup> and 247.10° from the model. As the barotropic flow is steered by the bathymetry, this result provides confidence in our representation of the bathymetry after the smoothing operation.

The Mariana region consists of two arc-shaped ridges: the main island arc is directly west of the trench subduction zone and a secondary arc is 250–300 km farther west. Modeled barotropic velocities are strongest between the islands on the southern portion of the main arc with major axis speeds of 8–12 cm s<sup>-1</sup>. Velocities over the northern portion of the arc typically reach 4–6 cm s<sup>-1</sup> with stronger velocities observed at the far northern islands (8 cm s<sup>-1</sup>). The western arc does not contain islands and maximum barotropic tidal velocities are 4–6 cm s<sup>-1</sup>.

#### b. $M_2$ internal tide field

Strong barotropic flow forced up and over the ridge systems at the Luzon Strait and Mariana Arc induces significant vertical velocities, displacing isopycnals, and generating internal waves that radiate away from the

ridges. Isopycnal displacements of over 50 m are found close to the generation region at the Luzon Strait and decrease as the waves propagate east. This compares with the vertical displacements modeled by Jan et al. (2008) and Niwa and Hibiya (2004). Vertical displacements of internal tides generated at the Mariana reach maximum values of 20 m in a focused beam along the arc's central axis. The internal tides have wavelengths of approximately 170 km and mode-1 propagates at 3.8 m s<sup>-1</sup>. Internal tides propagate along ray paths with a theoretical slope,  $s$  (the ratio of horizontal to vertical wavenumbers), given by

$$s = \pm \sqrt{\frac{\omega^2 - f^2}{N^2 - \omega^2}},$$

where  $\omega$  is the frequency of the internal wave,  $f$  is the inertial frequency, and  $N$  is the buoyancy frequency. The modeled wavelengths compare well with the wavelengths predicted by the theoretical ray paths calculated from the model buoyancy frequency profile. The wave speed in the model is consistent with the phase speed of the first baroclinic mode that is calculated to be 3.7 m s<sup>-1</sup> for the model's mean stratification. These values are also consistent with Niwa and Hibiya (2004) who simulated  $M_2$  internal tide wavelengths of 150–200 km and speeds of 3.5–4.5 m s<sup>-1</sup>.

The Luzon ridge spacing along 21°N is 122 km, which is similar wavelength to the  $M_2$  internal tides (Alford et al. 2011) and is nearly resonant. Figure 3 shows the baroclinic velocity structure and vertical isopycnal displacements along 21°N at the Luzon Strait for both maximum

westward and eastward barotropic velocity. Upward vertical displacement of isopycnals occurs when the barotropic tide flows up and over the ridges, with downward vertical displacement resulting on the lee side. When the flow reverses, vertical displacements reverse. Internal wave beams generated at each of the two ridges may be reinforced at the adjacent ridge as the ridge spacing is close to the wavelength of the internal tides (Farmer et al. 2009; Buijsman et al. 2012). This resonance may account for the greater vertical displacements modeled in the northern portion of the Strait. Further south at 20°N, the spacing ( $\sim 75$  km) is nonresonant for the  $M_2$  internal tides and vertical displacements to the east of the Strait are 32% smaller as compared to east of the resonant region to the north.

Internal tide generation is favored when the criticality (ratio of bottom slope to the characteristic ray path slope,  $s$ ) is greater than one. At the Luzon Strait the steepest model slopes occur on the eastern slope of the east ridge, reaching 0.15, while the western slope is less steep at around 0.07. The west ridge has a maximum topographic slope of 0.11 on both the east and west slopes. Criticality values, given the mean stratification, are greatest over the east ridge (ranging from about 1.75 to 3) and the eastern slope of the west ridge (1–2). At the Mariana Arc, model bathymetry bottom slopes range from 0.04 to 0.07 over most of the two arcs, and are between 0.08 and 0.11 on the southern portion of the eastern arc to the east and south of Guam. Criticality values are greatest on the eastern slope near Guam (up to 1.1) and at the far north where the two arcs converge (1–1.2). Criticality values across the domain show a strong qualitative correlation with regions of high internal tide generation.

### c. $M_2$ internal tide energetics

The conversion of barotropic tidal energy to baroclinic tides and the subsequent baroclinic processes can be described in terms of an energy budget. The barotropic energy flux is given by

$$\mathbf{F}_{bt} = \frac{1}{T_\theta} \int_0^{T_\theta} \int_{-H}^{\eta} \mathbf{u}_{bt\theta}(t) \rho_o g [\eta_\theta(t) - z] dz dt, \quad (2)$$

where  $\mathbf{u}_{bt\theta}$  is the barotropic velocity, and  $\eta_\theta$  is the surface elevation for the tidal period  $\theta$ . Upon interaction with steep topography, a portion of the barotropic tidal energy may be converted to baroclinic tidal energy with a typically small amount being lost to bottom friction or numerical dissipation. The radiation of internal tides from the generation site can be described as an energy flux. This baroclinic energy flux is calculated from the velocity and pressure perturbations which, following Nash et al. (2005), are given by

$$\mathbf{u}'_\theta(z, t) = \mathbf{u}_\theta(z, t) - \bar{\mathbf{u}}_\theta(z) - \bar{\mathbf{u}}_0(t), \quad (3)$$

and

$$p'_\theta(z, t) = p_\theta(z, t) - \bar{p}_\theta(z) - \bar{p}_0(t), \quad (4)$$

where  $\bar{\mathbf{u}}_\theta(z)$  and  $\bar{p}_\theta(z)$  are time mean quantities. The baroclinicity condition requires that the depth-averaged velocity and pressure perturbations vanish, such that

$$\bar{p}_0(t) = \frac{1}{H + \eta_\theta} \int_{-H}^{\eta_\theta} [p_\theta(z, t) - \bar{p}_\theta(z)] dz, \quad (5)$$

and

$$\bar{\mathbf{u}}_0(t) = \frac{1}{H + \eta_\theta} \int_{-H}^{\eta_\theta} [\mathbf{u}_\theta(z, t) - \bar{\mathbf{u}}_\theta(z)] dz. \quad (6)$$

The depth-integrated baroclinic flux is calculated from (3) and (4) via

$$\mathbf{F}_{bc} = \frac{1}{T_\theta} \int_0^{T_\theta} \int_{-H}^{\eta} \mathbf{u}'_\theta(z, t) p'_\theta(z, t) dz dt. \quad (7)$$

The barotropic to baroclinic energy conversion is calculated from the pressure perturbation at the bottom and the vertical component of the barotropic flow ( $w_{bt\theta}$ ), and is given by

$$C = \frac{1}{T_\theta} \int_0^{T_\theta} [p'_\theta(-H, t) w_{bt\theta}(-H, t)] dt, \quad (8)$$

where, assuming incompressibility,  $w_{bt\theta} = \mathbf{u}_{bt\theta} \cdot \nabla(-H)$ .

Because time snap shots of the model output can lead to undersampling of the tidal amplitudes, we compute the energy fluxes and conversion using spectral components. As such, Eq. (8) can be written in terms of the  $M_2$  amplitudes and Greenwich phases ( $\theta_{p'}$  and  $\theta_{w_{bt}}$ ) of  $p'(-H)$  and  $w_{bt}(-H)$ , as defined in Zilberman et al. (2011), as

$$C = 0.5 p'_{\theta A}(-H) w_{bt\theta A}(-H) \cos(\theta_{p'} - \theta_{w_{bt}}), \quad (9)$$

where the subscript  $A$  refers to the amplitudes.

Carter et al. (2008) partition the baroclinic energy into barotropic to baroclinic conversion ( $C$ ), tendency ( $T$ ), flux divergence ( $\nabla \cdot \mathbf{F}_{bc}$ ), nonlinear advection ( $A$ ), and dissipation ( $D$ ), where the baroclinic energy balance is defined as  $C = T + \nabla \cdot \mathbf{F}_{bc} + A + D$ . They define the baroclinic energy fluxes as in (7), and the conversion is dynamically equivalent to (8). The tendency term describes the time

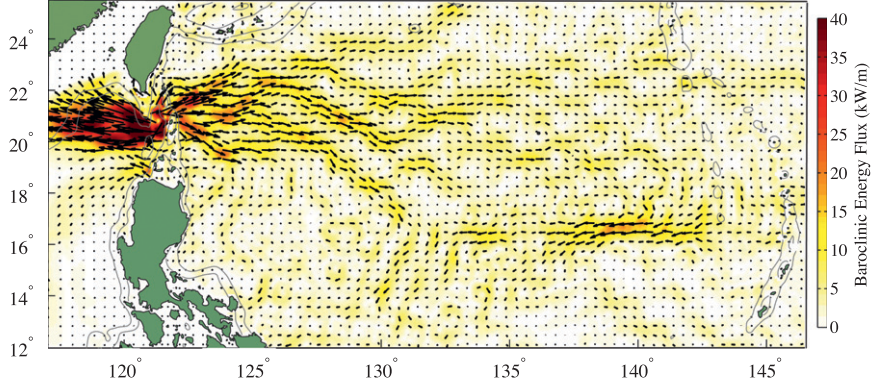


FIG. 4. Depth-integrated baroclinic energy fluxes for FULL model. Gray lines show 1000- and 2000-m depth contours.

rate of change of energy and is zero for a steady-state solution, and the advection term accounts for energy undergoing nonlinear transformations. Carter et al. (2008) show the tendency and advection terms are small for the Hawaiian Ridge, justifying the use of the dominant baroclinic energy balance  $D = C - \nabla \cdot \mathbf{F}_{bc}$ . This simplified energy budget approach has been employed in several other studies including Niwa and Hibiya (2004), Jan et al. (2008), and Zilberman et al. (2009). Alford et al. (2011) explicitly note that the dissipation  $D$  term accounts for all processes removing energy from the internal tide, including dissipation and nonlinear energy transfers. With modeling studies,  $D$  will also include numerical dissipation and error, and when computing the full balance, round-off errors, etc.

We examine the simplified energy budgets for both the Luzon Strait and Mariana Island Arc internal tide generation sites, characterizing the transfer of energy from the barotropic to the baroclinic tide, the radiation of baroclinic tide energy, and the internal tide energy lost locally. We define a bounding box for each of the two major conversion sites and calculate the residual energy, given by  $C - \nabla \cdot \mathbf{F}_{bc}$ , representing the losses from the internal tide by dissipation and nonlinear transfers (which we assume are small). As each site receives baroclinic energy fluxes that are generated remotely (outside of the bounding box) this residual energy accounts for the loss of both the locally converted baroclinic energy and the remotely generated internal tide energy within the bounding box, as well as any unresolved error. These two components cannot be separated and will be referred to collectively as residual baroclinic energy in this discussion.

Depth-integrated baroclinic energy fluxes for the FULL domain are shown in Fig. 4. Three distinct eastward beams are seen to the east of the Luzon Strait. The strongest flux is  $35 \text{ kW m}^{-1}$  propagating in a northeast

direction from the northern part of the Strait (where the ridge spacing is near-resonant). Decomposing the fluxes into modes, we find that 50% of the energy is in mode 2 that may be due to interaction of waves that are generated at both the western and eastern ridges. The eastward and southeastward beams are primarily generated over the Luzon eastern ridge with a maximum flux of  $20 \text{ kW m}^{-1}$  and  $25 \text{ kW m}^{-1}$ , respectively, and are composed of 80% mode-1 energy. East of  $126^\circ\text{E}$ , the fluxes form into three main southeastward-propagating beams that persist until  $131^\circ\text{E}$ . Fluxes generated at the Mariana Arc peak at  $20 \text{ kW m}^{-1}$  and propagate westward in a focused beam. This appears to be a result of the focusing of the arc-shaped generation site as discussed by Zhao and D'Asaro (2011), who reported fluxes of up to  $17 \text{ kW m}^{-1}$  in the beam.

Barotropic to baroclinic conversion over the entire domain for the FULL case is shown in Fig. 5, with energy budgets performed for the Luzon Strait and Mariana Arc conversion sites (defined by the blue dashed lines). Approximately 33% of the barotropic tidal energy ( $18.35 \text{ GW}$ ) is lost at the Luzon Strait, supporting  $16.97 \text{ GW}$  of barotropic to baroclinic energy conversion. The barotropic flux divergence is almost balanced by the barotropic to baroclinic conversion (93.5% converted) and the remaining  $1.38 \text{ GW}$  (7.5%) is attributed bottom friction losses. Here, 59% of the total conversion occurs at the eastern ridge and 41% at the western ridge. Our  $M_2$  conversion estimate is higher than those of Niwa and Hibiya (2004) ( $14 \text{ GW}$ ) and Jan et al. (2008) ( $9.6 \text{ GW}$ ). Jan et al. (2008) use a coarser resolution ( $\sim 9 \text{ km}$ ) compared to our  $4.5 \text{ km}$  over the Luzon Strait bathymetry, while Niwa and Hibiya (2004) find their conversion estimates are not sensitive to horizontal resolution (varied from  $1.7$  to  $7 \text{ km}$ ) although the topographic averaging radius was held constant at  $10 \text{ km}$ . Negative conversion values in Fig. 5 result from phase differences between the

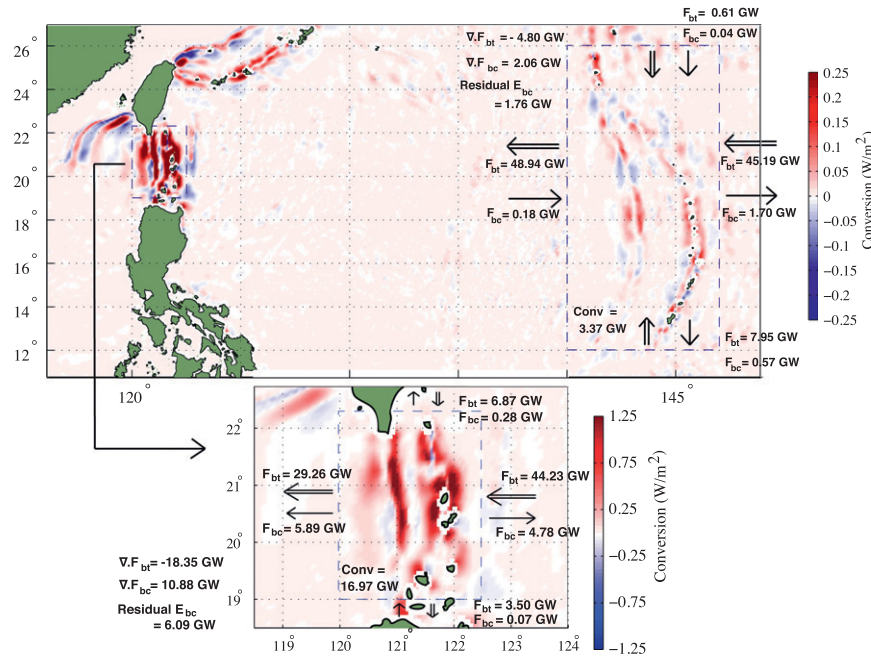


FIG. 5. Barotropic to baroclinic conversion for the FULL case. Energy budgets at the (bottom) Luzon Strait and Mariana Arc are shown for the boxes outlined by the blue dashed lines. Barotropic energy fluxes at the four sides are indicated by the double arrows, and baroclinic energy fluxes by the single arrows. Barotropic tide energy loss, total area-integrated tidal conversion, total baroclinic energy flux out, and residual baroclinic energy are given.

bottom pressure perturbation and the barotropic vertical velocity that are greater than  $90^\circ$  (Kurapov et al. 2003; Zilberman et al. 2009; Hall and Carter 2011; Carter et al. 2012). This occurs when nonlocally generated internal tides alter the phase of the pressure perturbation. In the case of the Luzon Strait, nonlocal internal tides are from distant generation sites such as the Mariana Arc as well as internal tides generated at the adjacent ridge. The total baroclinic energy flux out of the Luzon Strait bounding box is 10.88 GW. Of the energy flux leaving the box, 44% radiates to the east, 54% to the west, and the remainder is accounted for by fluxes in and out from the south and north. This is consistent with estimates by Niwa and Hibiya (2004) and Jan et al. (2008) who reported 43%–45% of the radiated baroclinic energy propagating eastward into the Philippine Sea. The residual baroclinic energy in our simulation is 6.09 GW. Assuming the remotely generated baroclinic energy fluxes entering the bounding box are small compared to those generated locally, this gives a local dissipation of 36% of the conversion.

A range of values of local dissipation at the Luzon Strait have been reported in previous modeling studies; however, the validity of these estimates is unclear as numerical models are unable to resolve subgrid-scale dissipative processes, and the spatial sparsity of observations make it difficult to verify model-estimated

energy budgets. Alford et al. (2011) reported 39% local dissipation for semidiurnal and diurnal bands and Niwa and Hibiya (2004) found 37% for  $M_2$  only. Additional simulations by Niwa and Hibiya (2004) applying an artificial linear damping term to the horizontal momentum equations to parameterize unresolved dissipative processes gave 47% local dissipation. Jan et al. (2008) use a similar parameterization to include additional damping and estimate 45%–46% for  $M_2$  with summer and winter stratifications and 57%–60% for semidiurnal and diurnal bands over the spring neap cycle. ROMS uses a quasi-monotone advection scheme, which consists of a high-order, integrally conservative, and nondissipative advection scheme followed by a locally adaptive correction such that numerical dispersion is transferred to diffusion (Shchepetkin and McWilliams 1998). We use harmonic viscosity to parameterize horizontal turbulence, and we find that the dissipation estimate at the Luzon Strait is not sensitive to the choice of coefficient. We varied the diffusion coefficient between  $1 \text{ m}^2 \text{ s}^{-1}$  and  $100 \text{ m}^2 \text{ s}^{-1}$  and the difference in resulting dissipation was less than 0.4%. The modeling study presented here does not use additional damping and our dissipation estimate is similar to those of Niwa and Hibiya (2004) and Alford et al. (2011) where damping is not included.

Dissipation may also be sensitive to the horizontal resolution of a model. Finite horizontal resolution limits the resolution of the higher vertical modes as singularities along tidal beams are smoothed and the conversion of baroclinic energy into these higher, more easily dissipated modes is suppressed. Di Lorenzo et al. (2006) attribute their reduced model conversion (as compared to the theoretical) to discretization and under representation of the higher modes. Sensitivity experiments by Niwa and Hibiya (2004) found dissipation estimates at the Luzon Strait were insensitive to horizontal resolution varied between 1.7 and 7 km (with a constant bathymetric averaging radius of 10 km). At the Mid-Atlantic Ridge, Zilberman et al. (2009) reported a higher resolution (1.5 km) gave a higher estimate of dissipation (52%), compared to 42% for the lower resolution (15 km) model. They found this was due to increased dissipation of the low modes owing to topographic scattering to higher modes in the lower resolution model.

The high dissipation at Luzon Strait has been attributed to the presence of the two ridges. Jan et al. (2008) compared the Luzon Strait dissipation for simulations with and without the western ridge and argue the strong dissipation of the semidiurnal tide is due to interference between rays generated at the two ridges. Buijsman et al. (2012) suggest that a potential mechanism for the increased dissipation is the formation of nonlinear internal hydraulic jumps, or high-mode turbulent lee waves. Alford et al. (2011) present dissipation values from observations and find that the spatial variability is consistent with model estimates, particularly in relation to the increased dissipation where the ridge spacing is resonant for the semidiurnal tide; however, sparse observations are not able to validate the regional energy budget.

At the Mariana Arc, only 7.1% of the incoming barotropic tidal energy is converted to baroclinic energy, compared to 33% at the Luzon Strait. Barotropic to baroclinic conversion at the Mariana Arc for the FULL case is shown in Fig. 5, and the area-integrated conversion over the bounding box is 3.82 GW. Barotropic energy loss over the region is 4.81 GW, leaving a residual of 0.99 GW lost to bottom friction, etc. The net baroclinic energy flux at the western edge of the box is eastward because of persistent eastward flux from the Luzon Strait dominating the westward flux generated at the Mariana Arc. The net flux radiated out of the box is 2.06 GW with 1.76 GW of baroclinic energy being lost within the box. This residual baroclinic energy includes the dissipation of the incoming flux from the Luzon Strait within the bounding box, as well as dissipation of locally generated internal tides.

#### 4. Effects of remotely generated internal tides

##### a. Conversion and energy budgets

Low-mode internal tides have been observed to travel thousands of kilometers across the oceans using satellite altimetry (Ray and Mitchum 1997; Ray and Cartwright 2001), current meters (Chiswell 2002; Alford 2003), and acoustics (Dushaw et al. 1995). The influence of remotely generated internal tides on local barotropic to baroclinic conversion has been studied for an idealized continental slope (Kelly and Nash 2010), for Monterey Submarine Canyon (Hall and Carter 2011), and for Hawaii (Zilberman et al. 2011; Powell et al. 2012). Changes in conversion result from interactions between remote and local internal tides that alter the magnitude and phase of the pressure perturbation at the bottom  $p'_\theta(-H, t)$ , with respect to the vertical barotropic velocity  $w_{bt\theta}(-H, t)$ , which remains the same. In the following section, we compare internal tide generation and propagation at the Luzon Strait and Mariana Arc from the FULL case with the LUZON (generation at the Luzon Strait with no baroclinic tides from the Mariana Arc) and the MARIANA (generation at the Mariana with no baroclinic tides from the Luzon Strait) cases.

Remotely generated internal tides from the Mariana Arc act to reduce the total conversion at the Luzon Strait in the model simulations. A comparison of conversion at the Luzon Strait plotted against longitude for the FULL case and the LUZON case is shown in Fig. 6, with the four primary conversion sites labeled. Conversion estimates are greater at the eastern ridge and the eastern slope of the western ridge, but relatively unaffected at the western slope of the western ridge. The total area-integrated conversion for the LUZON case increases by 1.83 GW (11%) to 18.80 GW in the absence of the Mariana Arc generated internal tides. Figure 7 shows the energy budget for the LUZON case (left panel) and the spatial conversion differences (LUZON–FULL, right panel). Positive difference values indicate greater conversion in the absence of the Mariana internal tide and negative values where conversion is increased by the remotely generated internal tides. Westward and eastward fluxes are 10% and 18% greater, respectively, compared to the FULL case. Residual baroclinic energy for the LUZON case is 6.34 GW, compared to 6.09 GW for the FULL case; as a percentage of local conversion this is only slightly less for the LUZON case (34% compared to 36%) suggesting local dissipation is dominant.

Barotropic to baroclinic conversion estimates at the Mariana Arc are significantly influenced by the internal tides generated at the Luzon Strait. Area-integrated conversion for the MARIANA case is 65% greater than

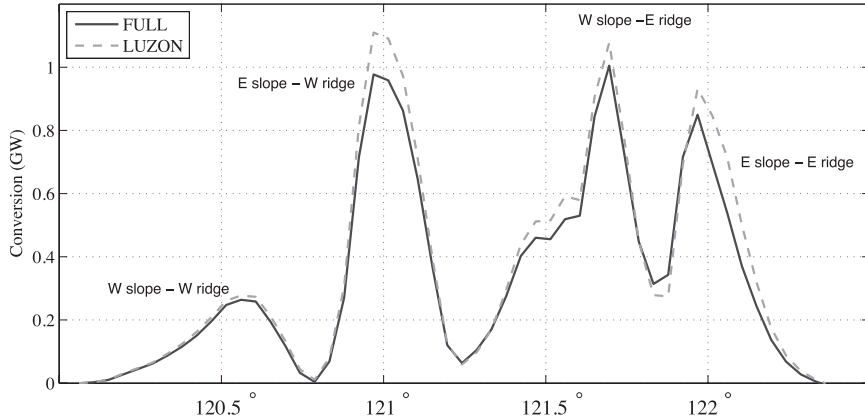


FIG. 6. Meridionally integrated tidal conversion at the Luzon Strait vs longitude for FULL domain and LUZON domain.

the FULL case (6.29 GW compared to 3.82 GW). Figure 8 shows the energy budget for the MARIANA case (left panel) and the difference in conversion (MARIANA–FULL, right panel) with positive values indicating greater conversion in the absence of remotely generated internal tides. There are significant changes to the conversion over the Mariana region for the MARIANA case with much fewer areas of “negative” conversion, compared to the FULL case (Fig. 5), as the phase of the bottom pressure perturbation is altered by the remotely generated internal tides in the FULL case.

At the western edge of the box, the net baroclinic flux is weakly eastward for the FULL case (0.18 GW) owing to persistence of flux from the Luzon Strait, while for the MARIANA case the flux is westward at 1.96 GW. At the eastern edge the total eastward flux is 11% greater for the MARIANA case because of increased conversion. The residual energy inside the bounding box is similar in both cases; 1.69 GW for the MARIANA case, compared to 1.76 GW for the FULL; however, in the FULL case this includes energy dissipated from the remotely generated fluxes as well as local dissipation. Because of the

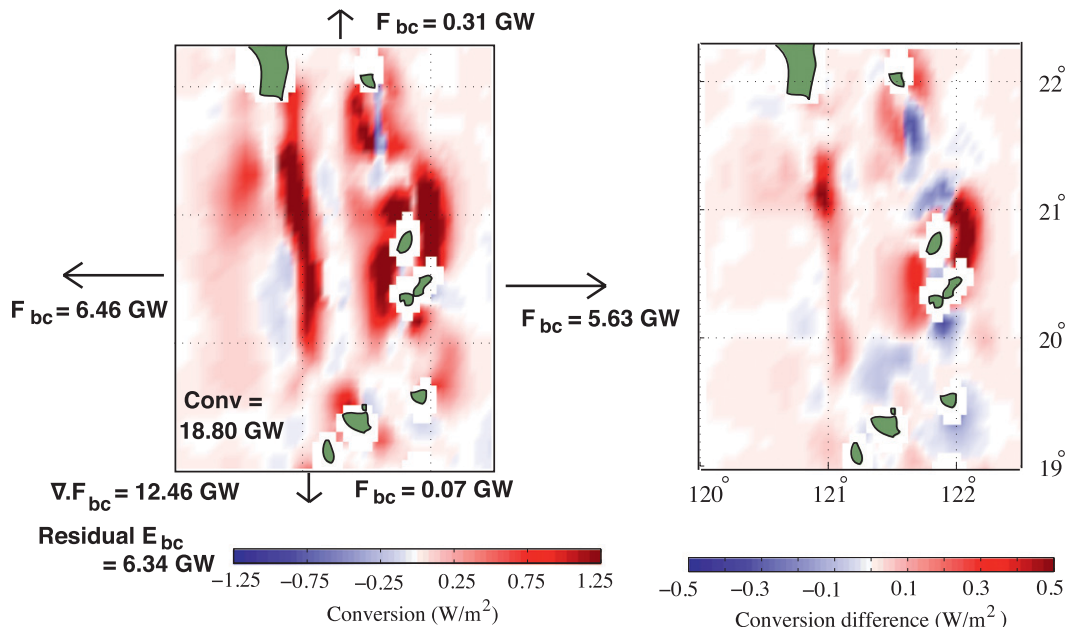


FIG. 7. Barotropic to baroclinic tidal energy conversion and energy budget for the (left) LUZON case and (right) conversion difference for LUZON–FULL cases. Positive difference values indicate where internal tides from the Mariana Arc have reduced conversion and vice versa.

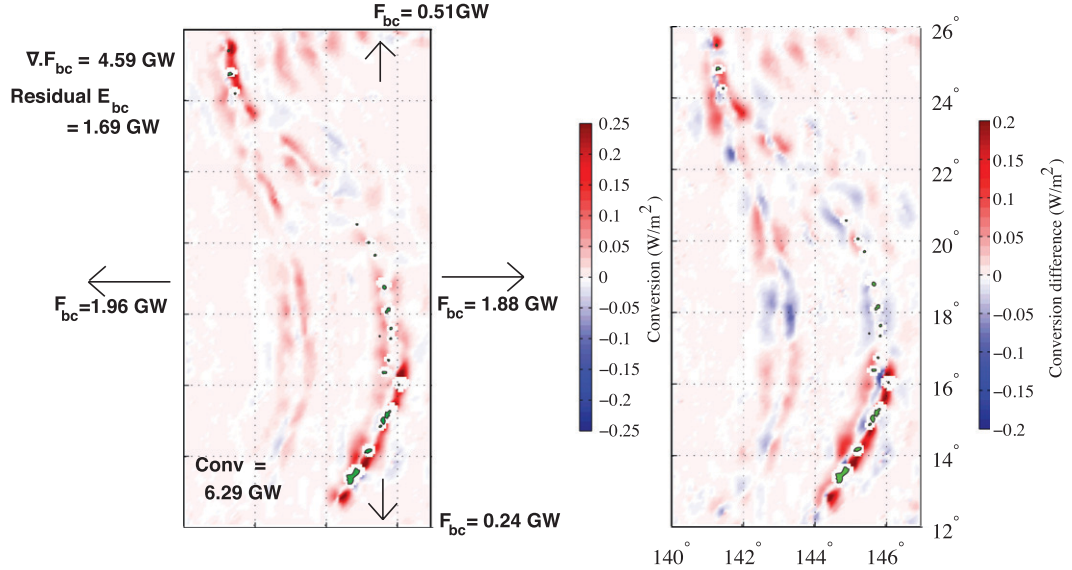


FIG. 8. Barotropic to baroclinic tidal energy conversion and energy budget for the (left) MARIANA case and (right) conversion difference for MARIANA–FULL cases. Positive difference values indicate where internal tides from the Luzon Strait have reduced conversion and vice versa.

absence of remote baroclinic energy in the MARIANA case we can equate this residual energy to local dissipation as a percentage of conversion, giving 27%.

The interaction of the opposing wave fields (from the Luzon Strait and the Mariana Arc) and the effect of remotely generated waves on local dissipation at the Mariana Arc are difficult to interpret. Buijsman et al. (2012) suggest that interactions between internal tides generated at the two ridges at the Luzon Strait drive dissipation via the formation of high-mode turbulent lee waves at the steep ridges; however, this mechanism is not likely to be relevant to the interactions of weaker fluxes over the more gentle topography at the Mariana Arc. It is noted that the eastward flux to the east of the Mariana Arc bounding box represents 30% of the total conversion for the MARIANA case, while for the FULL case the eastward flux is almost 45% of the local conversion (Figs. 5 and 7).

The modal composition of the baroclinic energy fluxes meridionally integrated across the domain reveals the superposition of opposing fluxes from the Luzon Strait and the Mariana Arc. Figure 9 shows the zonal baroclinic energy flux for the first three modes integrated from  $12^\circ$  to  $26^\circ\text{N}$ , for the FULL case (top panel) and the LUZON and MARIANA cases (bottom panel). In the FULL case, the mode-1 flux from the Luzon Strait persists across the Philippine Sea to the Mariana Arc and dominates over the westward mode-1 flux generated at the Mariana Arc generation site, total mode-2 and 3 fluxes are westward,

dominated by fluxes from the Mariana Arc. The modal composition to the east of the Mariana Arc differs in the FULL and MARIANA cases. The eastward flux at the eastern edge of the bounding box ( $147^\circ\text{E}$ ) in the MARIANA case is accounted for by the first three modes with 77%, 20%, and 3%, respectively. In the FULL case, while the energy flux from the Luzon Strait that reaches the Mariana Arc is dominantly mode 1, the net eastward flux on

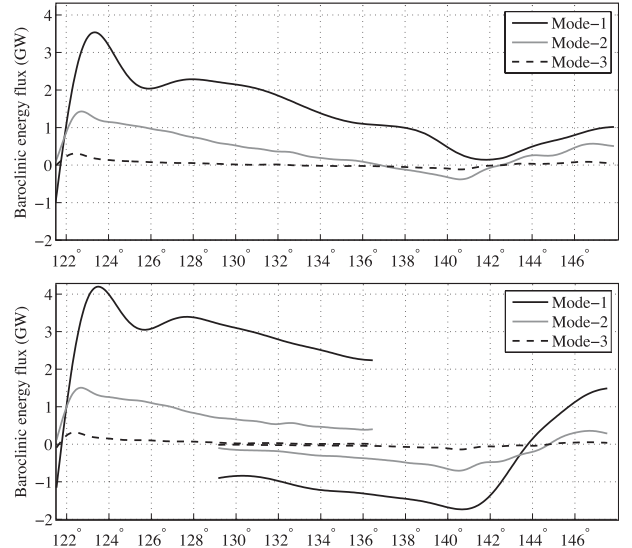


FIG. 9. The first three modes of the zonal baroclinic energy flux meridionally integrated between  $12^\circ$  and  $26^\circ\text{N}$  for the (top) FULL and (bottom) LUZON and MARIANA cases.

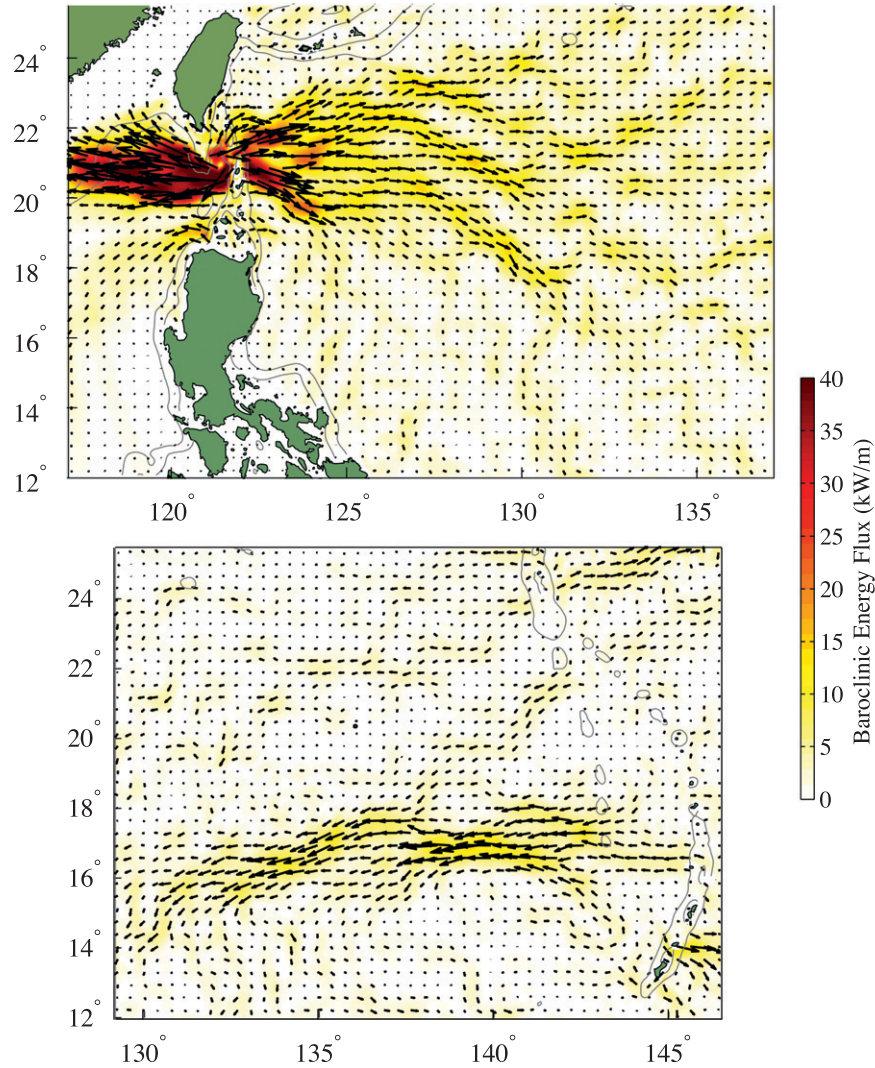


FIG. 10. Depth-integrated baroclinic energy fluxes for (top) LUZON case and (bottom) MARIANA case. Gray lines show 1000- and 2000-m depth contours. Compare to FULL case in Fig. 4.

the eastern side of the Mariana comprises more energy at higher modes as compared to the MARIANA case: 61% mode 1, 35% mode 2, and 4% mode 3. This suggests scattering of the eastward mode-1 flux from the Luzon Strait into higher modes at the Mariana Arc, similar to the findings by Johnston et al. (2003), which show the mode-1 energy emanating from the Hawaiian Ridge is scattered upon interaction with the Line Islands Ridge. This is significant as high-mode energy is dissipated more rapidly contributing to turbulent mixing.

The spatial pattern of the westward-propagating internal tides away from the Mariana Arc generation site obtained in the MARIANA simulation is altered by the superposition of the eastward-propagating flux from the Luzon Strait in the FULL case. Using satellite

altimetry, Zhao and D'Asaro (2011) observed a beam of zonal energy flux focused by the island chain near 17°N with a peak of energy near 140°E. Figure 10 shows the baroclinic energy fluxes from the LUZON and MARIANA cases, as compared to the FULL case in Fig. 4. In the FULL case, a single focused beam is found similar to Zhao and D'Asaro (2011). However, this is altered significantly when neglecting the effects of the Luzon. Significant conversion was shown to occur at both arcs (Fig. 5) and, in the MARIANA case, two focused beams persist at the focal points of the two arcs. This suggests that in addition to the focusing effects of the island arc as discussed by Zhao and D'Asaro (2011), remote effects are significant in the formation of a single, focused beam. The southeastward-propagating flux from

the Luzon Strait is particularly stronger in the LUZON case (reaching up to  $40 \text{ kW m}^{-1}$ ) compared to the FULL case (up to  $20 \text{ kW m}^{-1}$ ), corresponding to greater conversion on the eastern slope of the east ridge (Fig. 7). The southeastward beam is stronger than the northeastward beam in the LUZON case, while the opposite is true in the FULL case.

### b. Sensitivities and variability

The energy and phasing of the remote waves upon arrival at an internal tide generation site will influence their effect on local conversion. While higher modes typically dissipate close to their generation site, it is the low-mode internal waves that may travel significant distances reaching remote generation sites. As shown in the bottom panel of Fig. 9, very little energy at mode 3 reaches the edge of the LUZON and MARIANA domains. For the mean stratification used here, the times for modes 1–3 to travel along a chosen transect between the Luzon Strait and the Mariana Arc are 9.58, 19.1, and 28.91 days, respectively. For this reason, the simulations were integrated for 64 days. The presented analyses were from day 60 of the simulation to allow all modes cross the sea twice. This is necessary because, internal tides from the Luzon Strait cross the Philippine Sea to affect the conversion at the Mariana Arc and the resulting internal tides must be given time to propagate back across the domain.

To understand the impact on local conversion because of the arrival of the remote internal tides, the area-integrated conversion was calculated, averaged over 2 tidal cycles (24.84 h), for the entire period of the simulations for the Luzon Strait (FULL and LUZON domains) and the Mariana Arc (FULL and MARIANA domains) within the bounding boxes defined in Fig. 5. The difference in conversion at the Luzon Strait is shown in Fig. 11, illustrating how the arrival of each mode from the Mariana Arc affects the conversion for the FULL case compared to that of the LUZON case. The estimated mode arrival times are shown. The first significant internal waves are generated at the Mariana Arc after the first day of simulation, and this is added to estimated times for the modes to travel from the Mariana Arc. Conversion in the FULL and LUZON cases are the same prior to the arrival of mode-1 energy from the Mariana Arc ( $\sim 10$  days), indicating that our barotropic forcing in each model allows a valid comparison of remote effects. After the estimated arrival of mode-1 in the FULL case, the conversion decreases to 1.5 GW below the LUZON case. Around day 20, mode-2 energy arrives from the Mariana Arc. The energy in mode-1 is decreased after a decrease in conversion at the Mariana Arc (due to mode-1 waves from the Luzon Strait; mode-1 waves have crossed twice). The conversion initially increases and

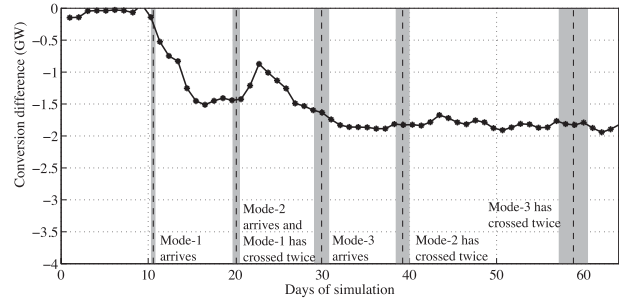


FIG. 11. Difference in area-integrated conversion at the Luzon Strait for the FULL and LUZON cases (FULL minus LUZON) with time of simulation. Black dashed lines show the arrival times of the first three modes of internal waves generated at the Mariana Arc as calculated from the mode speeds for the mean stratification used in the simulations. The gray bands show the variation in arrival time given seasonal and mesoscale variability (calculated from Mercator model output for 2010).

the combined effect is that conversion at the Luzon Strait thereafter proceeds to drop. A further decrease of  $\sim 0.3$  GW follows the arrival of mode-3, after which the conversion for the LUZON and FULL cases settles into a steady state with total a difference near 1.8 GW. Similarly, at the Mariana Arc (not shown), the area-integrated conversion is the same for the FULL and MARIANA cases before the arrival of mode-1, after which the FULL case decreases by 2.8 GW compared to the conversion for the MARIANA case. Between 20 and 30 days, mode-1 flux arriving from the Luzon Strait is reduced and the mode-2 waves arrive. Conversion for the FULL case increases by 0.3 GW, and after 30 days the difference between the FULL and MARIANA conversions remains constant at 2.5 GW.

This analysis provides insight into the influence of the important modes of remotely generated internal wave energy on the local conversion for a fixed stratification and helps quantify how each remotely generated mode affects local conversion; however, due to spatially and temporally varying stratification, significant uncertainties exist. The most important uncertainties regarding the remote effects are (i) the rate of decay of internal wave energy from its generation site, which directly affects how much energy will reach the remote site, and (ii) how mesoscale variability alters the propagation of various modes between sites and their phase upon arrival.

The amount of internal wave energy arriving at the remote site will be important in determining the pressure perturbation changes. In this simulation, we found that the first three modes affect remote conversion for the two opposing sites in the Philippine Sea, separated by  $\sim 2600$  km; however, the distance between the sites and the decay rate of the modes across the domain will

affect this. Direct observations of the dissipation of the internal tides are not available for the Philippine Sea. Observations of mode-1 internal tides propagating from the Hawaiian Ridge suggest negligible energy decay within 1000 km of the ridge (Rainville et al. 2010); although, the spatial variability due to complex interference patterns make single point observations difficult to interpret. Rainville et al. (2010) also found that simulations using the Princeton Ocean Model overestimated the high-mode energy, which may actually be more rapidly dissipated through wave–wave interactions and interaction with the mesoscale circulation (Rainville and Pinkel 2006). Factors that affect this decay in a numerical model include numerical dispersion and the choice of parameterization of mixing of momentum. In these simulations harmonic mixing of momentum was applied in the horizontal with a harmonic viscosity coefficient of  $50 \text{ m}^2 \text{ s}^{-1}$  and the results were not sensitive to this explicit diffusion. Simulations were conducted for the FULL case in which the coefficient was varied to  $1 \text{ m}^2 \text{ s}^{-1}$  and  $100 \text{ m}^2 \text{ s}^{-1}$ . Total conversion at the Luzon Strait was insensitive to this parameter, varying by no more than 0.4%. Conversion at the Mariana Arc was unchanged with the increased coefficient of  $100 \text{ m}^2 \text{ s}^{-1}$ . Decreasing the coefficient to  $1 \text{ m}^2 \text{ s}^{-1}$  resulted in a less than 2% decrease in conversion, which is insignificant compared to the 65% increase for the MARIANA simulation in which there was no internal tides from the Luzon Strait. Niwa and Hibiya (2004) found that additional damping in the horizontal was required for their model to achieve agreement of surface amplitudes with TOPEX/Poseidon satellite data. Further observations are required to determine the decay of internal tide energy away from generation regions and modeling studies, such as the one presented here, with varying distance between the sites or additional horizontal damping included would provide further insight into the sensitivity of remote effects to dissipation.

In this study, both generation sites showed decreased area-integrated conversion in the presence of remotely generated internal tides, but as seen in Figs. 7 and 8, increases and decreases in conversion vary spatially across the generation sites. This is caused by interactions between remote and local internal tides, which result in changes in both the magnitude and phase of the pressure perturbation at the bottom  $p'_\theta(-H, t)$ , with respect to the vertical barotropic velocity  $w_{bt\theta}(-H, t)$ . Kelly and Nash (2010) show that remotely generated internal tides can increase or decrease local generation depending on the phasing of the surface tide and the bottom pressure perturbation due to the internal tide. Equation (9) shows the dependence of the conversion on this phase

difference through the  $\cos(\theta_{p'} - \theta_{w_{bt}})$  term. The locally generated internal tide is forced by, and therefore coherent with, the surface tide. Remotely generated tides propagate through a dynamic ocean and may not be coherent with the local surface tides upon arrival at the new generation site. These phase changes affect how the remote waves will influence the local barotropic to baroclinic conversion through altering the phase difference. The conversion decreases as the phase difference increases from nearly zero (locally generated, coherent tides), and the conversion resolves as negative when the difference exceeds 90°.

The influence of remotely generated internal tides on the bottom pressure perturbations, which cause the conversion differences seen in Figs. 8 and 7, are shown in Figs. 12 and 13, respectively. In Fig. 12, the differences in bottom pressure perturbation amplitude and phase (MARIANA–FULL cases) are shown for all grid cells where conversion is greater than  $0.01 \text{ W m}^{-2}$ . The phase difference between  $w_{bt\theta}(-H, t)$  and  $p'_\theta(-H, t)$  is  $\sim 0^\circ$ – $45^\circ$  everywhere for the MARIANA case. Changes in the phase of the pressure perturbation of up to  $180^\circ$  are seen with the influence of remote waves from the Luzon Strait. At the Luzon Strait, differences in bottom pressure perturbation amplitude and phase (LUZON–FULL cases) are shown where conversion is greater than  $0.05 \text{ W m}^{-2}$  (Fig. 13). The phase differences have less effect on the conversion differences and changes to pressure perturbation amplitude dominate. In both cases, the changes in pressure perturbation amplitude and phase are spatially varying and complex highlighting the importance of including remote generation sites in regional modeling studies to achieve more valid conversion estimates. However, the phasing of the remotely generated internal tides upon reaching the local generation site will depend on the stratification through which they travel, so model simulations assuming mean stratification are not likely to correctly represent the phase changes.

The travel times of the internal tides across the domain between the Luzon Strait and the Mariana Arc for the mean stratification used in this study determine the phasing of the remote waves upon reaching the opposing generation site, but a different choice of stratification would present different results. Using model output from the Mercator general ocean circulation model for 2010, travel times of modes 1–3 vary by  $\sim 10$ , 18, and 39 h, respectively, owing to mesoscale variability (shown by gray bands in Fig. 11). As a travel time difference of 6.21 h (half the period of  $M_2$ ) would result in a complete  $180^\circ$  phase shift, the variability in travel times and the subsequent phase arrival due to mesoscale variability mean that the  $\cos(\theta_{p'} - \theta_{w_{bt}})$  term in Eq. (9) could vary anywhere between  $-1$  and  $1$ , varying spatially.

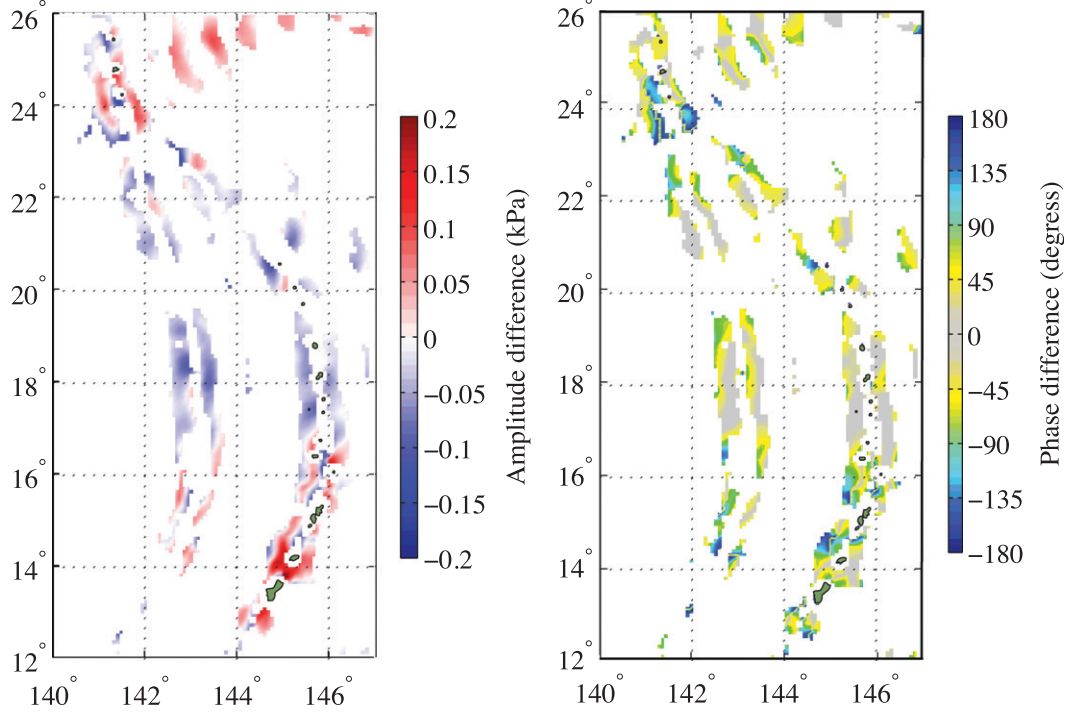


FIG. 12. Difference in bottom pressure perturbation (left) amplitude and (right) phase for the MARIANA and FULL cases (MARIANA–FULL). Only areas where conversion is greater than  $0.01 \text{ W m}^{-2}$  are shown. This illustrates how the remote internal tides significantly change the factors that determine conversion.

Mesoscale variability will also cause changes in stratification over the generation sites, affecting both the pressure perturbation induced by flow of the locally coherent barotropic tide over topography and the influence of the remote waves on the pressure perturbation amplitude.

We are currently conducting further research to understand how the local variability in internal tide generation depends on the locally changing mesoscale circulation and the varying influence of remotely generated waves, and the relative influence of each.

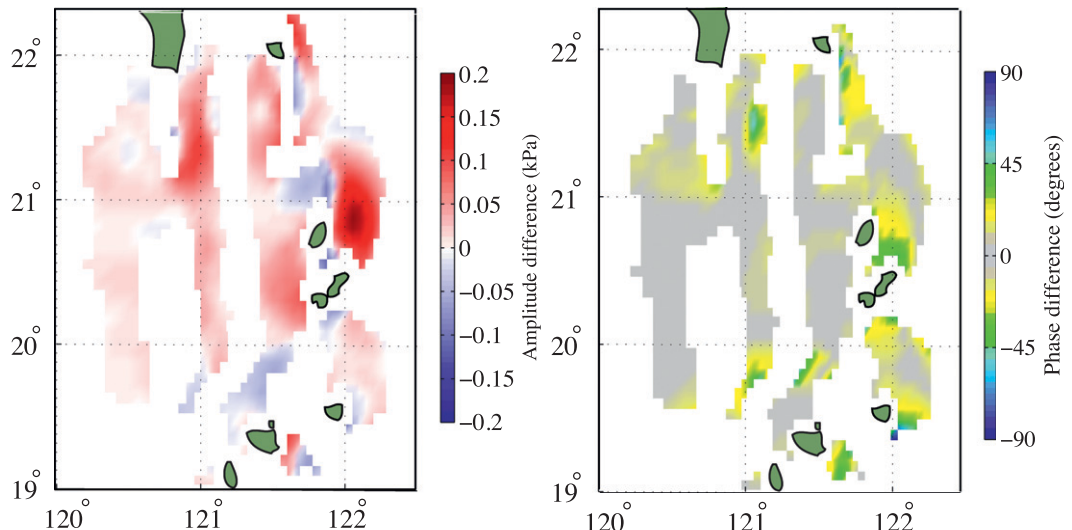


FIG. 13. Difference in bottom pressure perturbation (left) amplitude and (right) phase for the LUZON and FULL cases (LUZON–FULL). Only areas where conversion is greater than  $0.05 \text{ W m}^{-2}$  are shown. This illustrates how the remote internal tides change the factors that determine conversion.

## 5. Discussion

In this study, long-distance, remotely generated internal tides are found to have a significant influence on model estimates of internal tide energetics in the Philippine Sea. Regional numerical models are useful tools in the study of internal tide generation and propagation in the ocean, and while internal tide generation typically occurs at isolated regions of steep topography, studies should consider the potential effects of remotely generated internal tides in choosing appropriate model domains. Even in the case of a weak remote flux compared to the flux generated locally (e.g., the Luzon Strait in this study), remote effects on conversion estimates can be significant. In the presence of a strong remotely generated flux (e.g., the Mariana Arc in this study), local conversion and the propagation pattern of the radiating internal tides can be greatly altered.

Using the mean stratification and a domain that included both the Luzon Strait and Mariana Arc generation sites, we compared model simulations of the  $M_2$  internal tides. In the combined case, 16.97 GW of barotropic tide energy is converted to baroclinic energy at the Luzon Strait, with 4.78 GW propagating eastward into the Philippine Sea. On the eastern side of the Philippine Sea, the Mariana Island Arc converts 3.82 GW of energy from the surface tide to internal tides, which propagate westward in a focused beam.

Remote internal tides are found to affect barotropic to baroclinic conversion by altering the amplitude and phase of the bottom pressure perturbations in a complex, spatially varying pattern. For both sites, the total conversion increases when excluding the influence of remotely generated tides from the other. This influence depends on the amount of energy that reaches the site and the phase of the remote waves upon arrival. The flux from the Mariana Arc that reaches the Luzon Strait is weak compared to the locally generated flux; however, conversion at the Luzon Strait is increased by 11% when excluding internal tides generated at the Mariana Arc (a 1.83 GW difference) with the climatological stratification. The strong flux from the Luzon Strait most dramatically affects the energetics at the Mariana generation site. Conversion at the Mariana Arc for the simulation without the Luzon Strait generation site increases 65% without the Luzon Strait influence. The horizontal propagation patterns of the depth-integrated baroclinic energy fluxes from each site are also altered by the remotely generated fluxes.

These results are shown to affect observations of the region, as the combined case was consistent with the results of Zhao and D'Asaro (2011); however, when removing the influence of the Luzon Strait, the focused beam was weakened, which suggests that the shape of

the island arc is not the only amplifier for the focusing effect. Further observation studies will be better informed by employing modeling studies such as this to estimate the variability of the observed fluxes due to remote internal tides.

Mesoscale interactions were not simulated in this study with an assumed horizontally uniform stratification, and direct observations are required to validate decay rates achieved by parameterization of subgrid-scale dissipative processes. The time for internal tides to travel long distance differs as they travel through varying stratification and mesoscale circulation, affecting their phasing upon arrival. Given typical mesoscale variability, the time for modes 1 to 3 to travel across the Philippine Sea was calculated to vary by  $\sim$ 10, 20, and 40 h respectively, allowing for all possible phase changes. This complicates the picture as it makes the predictability of remote effects difficult. We found that because of the interaction that each site imparts on the other, combined with the variability of travel time across the basin, the conversion can vary significantly.

Low-mode internal tides may travel long distances across the ocean, and in this study the first three modes impact conversion at the opposing generation sites in the Philippine Sea, separated by  $\sim$ 2600 km. Martini et al. (2011) observed remote internal tides on the Oregon Shelf, and as shown by Simmons et al. (2004), there are few regions in the ocean that do not contain fluxes of internal tide energy. This work has implications for studies elsewhere, as global influence on regional conversion may be significant.

**Acknowledgments.** The authors thank the two anonymous reviewers for improving the original manuscript. Ms. Kerry and Dr. Powell were supported by The Office of Naval Research Grant N00014-09-10939. Dr. Carter was supported by NSF Grant OCN0825266. We thank I. Janešković for assisting with the model setup.

## REFERENCES

- Alford, M. H., 2003: Redistribution of energy available for ocean mixing by long-range propagation of internal waves. *Nature*, **423**, 159–163.
- , R.-C. Lien, H. Simmons, J. Klymak, S. Ramp, Y. J. Yang, D. Tang, and M.-H. Chang, 2010: Speed and evolution of nonlinear internal waves transiting the South China Sea. *J. Phys. Oceanogr.*, **40**, 1338–1355.
- , and Coauthors, 2011: Energy flux and dissipation in Luzon Strait: Two tales of two ridges. *J. Phys. Oceanogr.*, **41**, 2211–2222.
- Bergh, J., and J. Berntsen, 2009: Numerical studies of wind forced internal waves with a nonhydrostatic model. *Ocean Dyn.*, **59**, 1025–1041.
- Buijsman, M. C., S. Legg, and J. Klymak, 2012: Double ridge internal tide interference and its effect on dissipation in Luzon Strait. *J. Phys. Oceanogr.*, **42**, 1337–1356.

- Carter, G. S., and Coauthors, 2008: Energetics of  $M_2$  barotropic-to-baroclinic tidal conversion at the Hawaiian Islands. *J. Phys. Oceanogr.*, **38**, 2205–2223.
- , O. B. Fringer, and E. D. Zaron, 2012: Regional models of internal tides. *Oceanography (Wash. D.C.)*, **25**, 56–65.
- Chapman, D. C., 1985: Numerical treatment of cross-shelf open boundaries in a barotropic coastal ocean model. *J. Phys. Oceanogr.*, **15**, 1060–1075.
- Chiswell, S. M., 2002: Energy levels, phase, and amplitude modulation of the baroclinic tide off Hawaii. *J. Phys. Oceanogr.*, **32**, 2640–2651.
- Cummins, P. F., and L.-Y. Oey, 1997: Simulation of barotropic and baroclinic tides off Northern British Columbia. *J. Phys. Oceanogr.*, **27**, 762–781.
- Di Lorenzo, E., W. R. Young, and S. L. Smith, 2006: Numerical and analytical estimates of  $M_2$  tidal conversion at steep oceanic ridges. *J. Phys. Oceanogr.*, **36**, 1072–1084.
- Duda, T. F., J. F. Lynch, J. D. Irish, R. C. Beardsley, S. R. Ramp, C.-S. Chiu, T. Y. Tang, and Y.-J. Yang, 2004: Internal tide and nonlinear internal wave behaviour at the continental slope in the northern South China Sea. *J. Ocean. Eng.*, **29**, 1105–1130.
- Dushaw, B. D., B. D. Cornuelle, P. F. Worcester, B. M. Howe, and D. S. Luther, 1995: Barotropic and baroclinic tides in the central North Pacific Ocean determined from long-range reciprocal acoustic transmissions. *J. Phys. Oceanogr.*, **25**, 631–647.
- Egbert, G. D., and R. D. Ray, 2000: Significant dissipation of tidal energy in the deep ocean inferred from satellite altimeter data. *Nature*, **405**, 775–778.
- , and —, 2001: Estimates of  $M_2$  tidal energy dissipation from TOPEX/Poseidon altimeter data. *J. Geophys. Res.*, **106** (C10), 22 475–22 502.
- , and S. Y. Erofeeva, 2002: Efficient inverse modeling of barotropic ocean tides. *J. Atmos. Oceanic Technol.*, **19**, 183–204.
- Farmer, D., Q. Li, and H.-H. Park, 2009: Internal wave observations in the South China Sea: The role of rotation and nonlinearity. *Atmos.–Ocean*, **47**, 267–280.
- , M. H. Alford, R.-C. Lien, Y. J. Yang, M.-H. Chang, and Q. Li, 2011: From Luzon to Dongsha Plateau—Stages in the life of an internal wave. *Oceanography*, **24**, 64–77.
- Flather, R. A., 1976: A tidal model of the northwest European continental shelf. *Mem. Soc. Roy. Sci. Liege*, **6**, 141–164.
- Haidvogel, D. B., H. G. Arango, K. Hedstrom, A. Beckmann, P. Malanotte-Rizzoli, and A. F. Shchepetkin, 2000: Model evaluation experiments in the North Atlantic Basin: Simulations in nonlinear terrain-following coordinates. *Dyn. Atmos. Oceans*, **32**, 239–281.
- Hall, R. A., and G. S. Carter, 2011: Internal tides in Monterey submarine canyon. *J. Phys. Oceanogr.*, **41**, 186–204.
- Haney, R. L., 1991: On the pressure gradient force over steep topography in sigma coordinate ocean models. *J. Phys. Oceanogr.*, **21**, 610–619.
- Holloway, P. E., 1987: Internal hydraulic jumps and solitons at a shelf break region on the Australian north west shelf. *J. Geophys. Res.*, **92** (C5), 5405–5416.
- Intergovernmental Oceanographic Commission, 2003: Centenary edition of the GEBCO Digital Atlas. British Oceanographic Data Centre, CD-ROM.
- Jan, S., R.-C. Lien, and C.-H. Ting, 2008: Numerical study of baroclinic tides in Luzon Strait. *J. Oceanogr.*, **64**, 789–802.
- Jefferies, H., 1920: Tidal friction in shallow seas. *Philos. Trans. Roy. Soc. London*, **A221**, 239–264.
- Johnston, T. M. S., M. Merrifield, and P. Holloway, 2003: Internal tide scattering at the Line Islands Ridge. *J. Geophys. Res.*, **108**, 3365, doi:10.1029/2003JC001844.
- Kelly, S. M., and J. D. Nash, 2010: Internal-tide generation and destruction by shoaling internal tides. *Geophys. Res. Lett.*, **37**, L23611, doi:10.1029/2010GL045598.
- Klymak, J. M., R. Pinkel, and L. Rainville, 2007: Direct breaking of the internal tide near topography: Kaena Ridge, Hawaii. *J. Phys. Oceanogr.*, **38**, 380–399.
- , M. H. Alford, R. Pinkel, R.-C. Lien, Y. J. Yang, and T.-Y. Tang, 2010: The breaking and scattering of internal tide on a continental slope. *J. Phys. Oceanogr.*, **41**, 926–945.
- Kurapov, A. L., G. D. Egbert, J. S. Allen, R. N. Miller, S. Y. Erofeeva, and P. M. Kosro, 2003: The  $M_2$  internal tide off Oregon: Inferences from data assimilation. *J. Phys. Oceanogr.*, **33**, 1733–1757.
- Large, W. G., J. C. McWilliams, and S. Doney, 1994: Oceanic vertical mixing: A review and a model with a nonlocal boundary layer parameterization. *Rev. Geophys.*, **32**, 363–403.
- Liao, G., Y. Yuan, K. Arata, C. Yang, H. Chen, T. Noakazu, G. Noriaki, and M. Masanori, 2010: Analysis of internal tidal characteristics in the layer above 450 m from acoustic Doppler current profiler observations in the Luzon Strait. *Sci. China Ser. B*, **54D**, 1078–1091.
- Lien, R. C., T. Y. Tang, M. H. Chang, and E. A. D’Asaro, 2005: Energy of nonlinear internal waves in the South China Sea. *Geophys. Res. Lett.*, **32**, L05615, doi:10.1029/2004GL022012.
- Martini, K. I., M. H. Alford, E. Kunze, S. M. Kelly, and J. D. Nash, 2011: Observations of internal tides on the Oregon continental slope. *J. Phys. Oceanogr.*, **41**, 1772–1794.
- Mellor, G. L., T. Ezer, and L. Y. Oey, 1994: The pressure gradient conundrum of sigma coordinate ocean models. *J. Atmos. Oceanic Technol.*, **11**, 1126–1134.
- Merrifield, M. A., and P. E. Holloway, 2002: Model estimates of  $M_2$  internal tide energetics at the Hawaiian Ridge. *J. Geophys. Res.*, **107**, 3179, doi:10.1029/2001JC000996.
- Munk, W., and C. Wunsch, 1998: Abyssal recipes II: Energetics of tidal and wind mixing. *Deep-Sea Res.*, **45**, 1977–2010.
- Nash, J. D., M. H. Alford, and E. Kunze, 2005: Estimating internal wave energy fluxes in the ocean. *J. Atmos. Oceanic Technol.*, **22**, 1551–1570.
- Niwa, Y., and T. Hibiya, 2001: Numerical study of the spatial distribution of the  $M_2$  internal tide in the Pacific Ocean. *J. Geophys. Res.*, **106** (C10), 22 441–22 449.
- , and —, 2004: Three-dimensional numerical simulation of  $M_2$  internal tides in the East China Sea. *J. Geophys. Res.*, **109**, C04027, doi:10.1029/2003JC001923.
- Powell, B. S., I. Janevic, G. S. Carter, and M. A. Merrifield, 2012: Sensitivity of internal tide generation in Hawaii. *Geophys. Res. Lett.*, **39**, L10606, doi:10.1029/2012GL051724.
- Rainville, L., and R. Pinkel, 2006: Propagation of low-mode internal waves through the ocean. *J. Phys. Oceanogr.*, **36**, 1220–1236.
- , T. M. S. Johnston, G. S. Carter, M. A. Merrifield, R. Pinkel, P. F. Worcester, and B. D. Dushaw, 2010: Interference pattern and propagation of the  $M_2$  internal tide south of the Hawaiian Ridge. *J. Phys. Oceanogr.*, **40**, 311–325.
- Ramp, S. R., and Coauthors, 2004: Internal solitons in the northeastern South China Sea Part 1: Sources and deep water propagation. *J. Ocean. Eng.*, **29**, 1157–1181.
- Ray, R. D., and G. T. Mitchum, 1997: Surface manifestation of internal tides in the deep ocean: Observations from altimetry and island gauges. *Prog. Oceanogr.*, **40**, 135–162.

- , and D. E. Cartwright, 2001: Estimates of internal tide energy fluxes from Topex/Poseidon altimetry: Central North Pacific. *Geophys. Res. Lett.*, **28**, 1259–1262.
- Shchepetkin, A. F., and J. C. McWilliams, 1998: Quasi-monotone advection schemes based on explicit locally adaptive dissipation. *Mon. Wea. Rev.*, **126**, 1541–1580.
- , and —, 2003: A method for computing horizontal pressure-gradient force in an oceanic model with a nonaligned vertical coordinate. *J. Geophys. Res.*, **108**, 3090, doi:10.1029/2001JC001047.
- , and —, 2005: The regional oceanic modeling system (ROMS): A split-explicit, free-surface, topography-following-coordinate oceanic model. *Ocean Modell.*, **9**, 347–404.
- Sikiric, M. D., I. Janevic, and M. Kuzmic, 2009: A new approach to bathymetry smoothing in sigma-coordinate ocean models. *Ocean Modell.*, **29**, 128–136.
- Simmons, H. L., R. W. Hallberg, and B. K. Arbic, 2004: Internal wave generation in a global baroclinic tide model. *Deep-Sea Res. II*, **51**, 3043–3068.
- Vitousek, S., and O. B. Fringer, 2011: Physical vs. numerical dispersion in nonhydrostatic ocean modeling. *Ocean Modell.*, **40**, 72–86.
- Wajsowicz, R. C., 1993: A consistent formulation of the anisotropic stress tensor for use in models of the large-scale ocean circulation. *J. Comput. Phys.*, **105**, 333–338.
- Zhao, Z., and E. D’Asaro, 2011: A perfect focus of the internal tide from the Mariana Arc. *Geophys. Res. Lett.*, **38**, L14609, doi:10.1029/2011GL047909.
- , V. Klemas, Q. Zheng, and X.-H. Yan, 2004: Remote sensing evidence for baroclinic tide origin of internal solitary waves in the northeastern South China Sea. *Geophys. Res. Lett.*, **31**, L06302, doi:10.1029/2003GL019077.
- Zilberman, N. V., J. M. Becker, M. A. Merrifield, and G. S. Carter, 2009: Model estimates of  $M_2$  internal tide generation over mid-Atlantic ridge topography. *J. Phys. Oceanogr.*, **39**, 2635–2651.
- , M. A. Merrifield, G. S. Carter, D. S. Luther, M. D. Levine, and T. J. Boyd, 2011: Incoherent nature of  $M_2$  internal tides at the Hawaiian Ridge. *J. Phys. Oceanogr.*, **41**, 2021–2036.